Self-archived version of the article published in Desalination:
M. Micari, A. Cipollina, F. Giacalone, G. Kosmadakis, M. Papapetrou, G. Zaragoza, G. Micale, A. Tamburini, Towards the first proof of concept of a Reverse ElectroDialysis Membrane Distillation Heat Engine, Desalination, Volume 453, 1 March 2019, Pages 77-88,
https://doi.org/10.1016/j.desal.2018.11.022

Towards the first proof of concept of a Reverse ElectroDialysis – Membrane Distillation Heat Engine

M. Micari[a, c], A. Cipollina[a], F. Giacalone[a], G. Kosmadakis[e], M. Papapetrou[a,e], G. Zaragoza[b,d], G. Micale[a*], A. Tamburini[a]

[a] *Dipartimento dell'Innovazione Industriale e Digitale (DIID) - Ingegneria Chimica, Gestionale, Informatica, Meccanica, Università di Palermo (UNIPA) – viale delle Scienze Ed.6, 90128 Palermo, Italy.*

[b] *CIEMAT-Plataforma Solar de Almería, Ctra. de Senés s/n, Tabernas, Almería, Spain.*

[c] *German Aerospace Center (DLR), Institute of Engineering Thermodynamics, Pfaffenwaldring 38-40, 70569 Stuttgart, Germany.*

[d] *German Aerospace Center (DLR), Institute of Solar Research, Ctra. de Senés s/n, Tabernas, Almería, Spain.*

[e] *Wirtschaft und Infrastruktur GmbH & Co Planungs-KG (WIP), Sylvensteinstr. 2, 81369 Munich, Germany.*

[*] *Corresponding author: giorgiod.maria.micale@unipa.it*

Abstract

The coupling of Reverse Electrodialysis with Membrane Distillation is a promising option for the conversion of waste heat into electricity. This study evaluates the performances of the integrated system under different operating conditions, employing validated model and correlations. This work provides a detailed description of the behaviour of a real RED-MD heat engine and indicates the set of inlet concentrations, velocities and equipment size which returns the highest cycle exergy efficiency. These operating conditions were selected for the pilot plant developed within the EU-funded project RED Heat to Power. For the first time, a perspective analysis was also included, considering highly performing RED membranes and future MD module. Relevant results indicate that technological improvements may lead to interesting system performance enhancement, up to an exergy efficiency of 16.5%, which is considerably higher than the values reported in literature so far.

Keywords

Reverse Electrodialysis Heat Engine; Reverse Electrodialysis; Membrane Distillation; Waste heat recovery; Salinity Gradient Power

1. Introduction and literature review

Nowadays, an increasing research interest is devoted to the exploitation of salinity gradient energy, i.e. the chemical energy associated to the mixing of two solutions at different salt concentration. Among the SGP technologies, two have reached a significantly high technology readiness level, namely Pressure Retarded Osmosis (PRO) and Reverse Electrodialysis (RED) [1–5]. The former employs membranes, which are selective toward the passage of the solvent, while the latter is based on membranes which are selective toward the passage of ions. Wide comparisons between PRO and RED performances in different operating conditions are available in literature [6–8]. Notably, two advantages of the RED process concern the fact that: (i) it generates directly electricity instead of mechanical energy which has to be converted into electricity; and (ii) RED membranes are, in general, less sensitive to fouling than PRO ones [6].

Focusing on RED technology, it can operate in an open-loop, using natural streams (e.g. seawater and river water) [9] or streams deriving from human activities as desalination plants, saltworks or sewage treatment plants [10]. Otherwise, RED units can operate inside a closed-loop, coupled with a regeneration section, where heat (typically waste heat) is supplied to restore the initial salinity gradient [7]. In this way a salinity gradient heat engine can be devised. As a result, low temperature heat (low-grade waste heat, low-temperature renewable heat source) can be converted into electricity. This follows the growing industrial interest in taking advantage of the large amount of unexploited low-grade waste heat with the aim of increasing the overall energetic efficiency of production cycles [11,12].

This idea is the key concept of the EU-funded project RED Heat-to-Power [13], whose goal is the development of a RED Heat Engine (REDHE), which consists of two main parts. The first one is the “energy generation” section, where electricity is produced inside the Reverse Electrodialysis unit. Two solutions at different concentrations are fed to the stack, which is composed of a series of ion exchange membranes, arranged in an alternate way. The second part is the “regeneration” section, where the two exhausted solutions, exiting from the stack, are brought back to their initial concentration, in order to restore the salinity gradient and close the cycle. Two different schemes have been devised for coupling the two sections of Reverse Electrodialysis Heat Engine (REDHE): the “solvent-extraction” scheme and the “salt-extraction” scheme [11], which are illustrated in Figure 1.

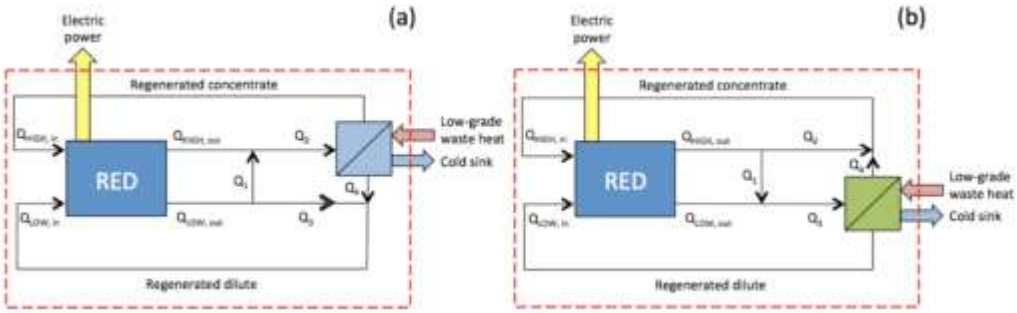

Figure 1. REDHE possible schemes: RED coupled with a solvent extraction strategy (a) and with a salt extraction strategy (b) [14].

The first scheme consists of a RED unit coupled with a thermally-driven technology, which recovers the solvent from the outlet concentrate solution (Figure 1a). In this case, the outlet concentrate solution, exiting from the stack, is mixed with a fraction of the outlet dilute solution, in order to restore its salt content that was lost during the RED process. This resulting stream is sent to the regeneration stage in order to recover the solvent in excess and restore the initial concentration level of the concentrate solution. The solvent extracted is added to the outlet dilute stream, which is thus restored to its initial condition. The regeneration technology can be an evaporative process (e.g. Multiple Effect Distillation (MED) [15,16] or Membrane Distillation (MD) [17–19]) or another process like Forward Osmosis (FO) provided with a temperature-sensitive drawing agent [20].

The second scheme provides the coupling of the RED stack with a salt-extraction process (Figure 1b), which recovers the solute (i.e. the salt) from the outlet dilute solution. In this case, the outlet dilute solution is mixed with a fraction of the outlet concentrate solution, in order to balance the solvent exchanged due to osmotic effects. Then, this solution is sent to the regeneration process, in which the salt in excess is extracted either by variation of salt solubility (using switchable-solubility salts [21]) or by salt degradation (using thermolytic salts [22–25]).

Among the mentioned REDHE configurations, this work is focused on a "solvent extraction scheme" heat engine where the RED stack is coupled with a Membrane Distillation unit. In particular, this idea started from the necessity to identify a viable configuration for a pilot plant of the RED-MD integrated system, within the framework of the RED Heat-to-Power project [13]. Membrane Distillation is particularly advantageous for its modularity and operational simplicity, which make it suitable for being operated at any scale, from the lab-scale up to the industrial level [26]. For this

reason, the choice to couple the RED process with MD is particularly suitable for a small-scale pilot plant, representing the *proof of concept* of this SGP heat engine.

This marks a significant difference from MED, since MED is intrinsically a large-scale technology. Therefore, MED cannot be scaled-down to less than several hundreds of m^3/day, i.e. a scale much larger than the laboratory one [27]. However, the energy consumption of the MD process is higher than that of MED: in literature the reported specific thermal consumption is hardly below around 100-200 $kWh/m^3_{distillate}$ for MD [28], while for MED it can reach values as low as 50-70 $kWh/m^3_{distillate}$ [15]. Clearly, this difference would determine a decrease of the cycle efficiency and for this reason, MD turns out to be a competitive and cost-effective technology when low cost thermal energy is available [19,29], as in the case under investigation. Moreover, the MD process requires a lower vapour space than the MED process [30]. Furthermore, since MD is a relatively new process with respect to the MED technology, it is expected to undergo continuous developments in the next years, hopefully reaching higher thermal efficiencies at lower costs. The potential of MD and its thermodynamic limits has been extensively discussed and reported in literature. Different MD unit configurations were investigated [17,31], detailed theoretical model were proposed and validated [32] and the potential of the coupling of MD with renewable energy sources was assessed [27]. However, some challenges have still to be faced, such as the reduction of the conductive thermal losses and the minimization of temperature polarization in order to enhance the thermal efficiency [26,27].

The RED process has been widely investigated with the aim of identifying optimal operating conditions and maximum producible power-output. Scientific efforts were focused on the overall system design [33,34], on the fluid-dynamics within the channels [35] or on the electrode material investigation [36]. Several studies are also focused on the development of Ionic Exchange Membranes with low electrical resistance and high perm-selectivity [37], on the investigation of membrane materials [38,39] and on the specific interactions between membrane and ions in the solution [40,41].

As far as the coupling of SGP technologies with MD is concerned, only very few studies are reported in literature. Lin et al. [42] carried out a theoretical study on the performances of an Osmotic Heat Engine (OHE), resulting from the coupling of Pressure Retarded Osmosis (PRO) with MD and operating with NaCl-water solutions. The OHE overall efficiency was estimated under several mass and heat transfer regimes in the regeneration stage. The temperature of the heat source, the concentration of the

solution fed to the MD unit and the inlet distillate to feed flow rate ratio were identified as the parameters mostly affecting the process performance. Another study on the PRO-MD system concerned the use of LiCl-water or LiCl-methanol solutions [43]. A recent study [44] investigated the RED-MD heat engine fed by NaCl and water, evaluating the cycle efficiency dependence on the heat source temperature, the NaCl concentration of the MD feed (varying from 1 mol/kg to 5 mol/kg) and the ratio between inlet permeate and feed solution flow rate. In this study, a direct contact MD is coupled with a RED unit, and the maximum achievable energetic efficiency is around 1.15% (corresponding to an exergy efficiency of 9.6%). Finally, another study presented a combination of MD and RED technology to treat the retentate exiting from a seawater reverse osmosis desalination plant, with the aim of producing simultaneously energy and desalted water [45].

The present work aims at performing a parametric study of the RED-MD integrated system by referring to real existing units in order to develop the first proof of concept of the RED-MD heat engine. Both Reverse Electrodialysis and Membrane Distillation are described combining theoretical validated models and data from commercial MD units provided by Aquastill®. The power generated by the RED unit considers the limitations due to real membrane properties (i.e. electrical resistance, permselectivity, water and salt fluxes). The correlations relevant to the MD unit are derived from a validated model and refer to the real MD working range of operating concentrations, limited by the decrease of the driving force, especially for long MD units. Overall, the aim of the work is to show the potential of the integrated RED-MD system, accounting for real equipment. Moreover, a perspective analysis was carried-out in order to investigate the performance of future RED-MD HE, considering highly performing RED membranes and MD units, providing the resulting LCOE as a function of the RED and MD specific costs.

2. Mathematical modelling

The layout of the coupled RED-MD system is sketched in Figure 2. The integrated system was designed considering the two processes as connected in a discontinuous way, due to the different scale (or working times) of the two units employed, a commercial RED stack and commercial MD modules.

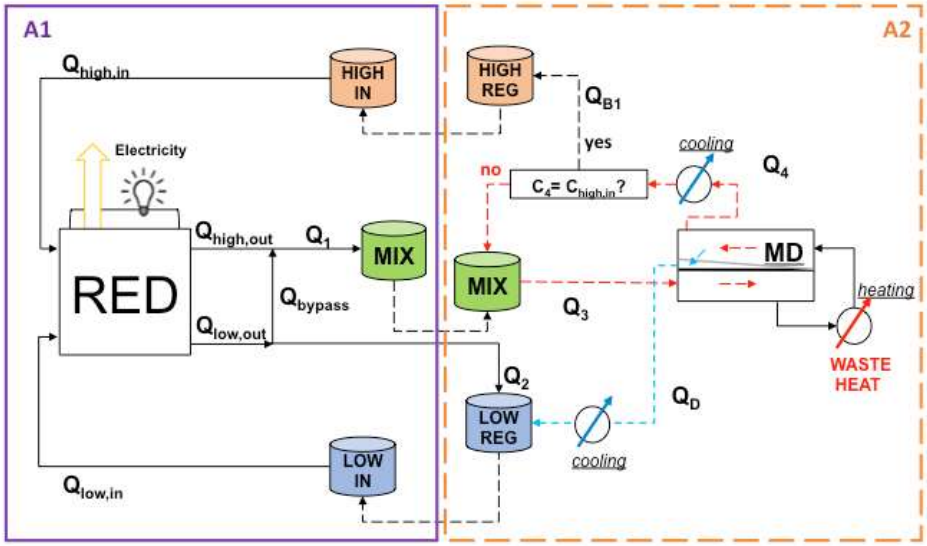

Figure 2. RED-MD integrated system. The area inside the purple-solid rectangle (A1) works in continuous while the area inside the orange-broken rectangle (A2) works in batch conditions. Dashed lines refer to batch operations while continuous lines refer to continuous operations.

More precisely, the whole system operates cyclically. In each working cycle, the RED unit is supposed to work in continuous for 5 h, during that a dilute and concentrate solutions are fed in the unit with fixed flow rates ranging from 10 to 50 l/h. The outlet concentrate solution ($Q_{high,out}$) is mixed with a fraction of the outlet dilute solution (Q_{bypass}), in order to restore the initial content of salt (see Figure 2). The resulting solution volume is accumulated in the MIX tank during the RED working time. This volume is recirculated within the MD unit up to the achievement of the desired concentration ($C_{high,in}$) with a fixed flow rate of 600 l/h (typical of commercial MD modules). Then, the MD working time (t_{MD}) depends on the RED outlet concentrations. This working time, typically in the range of 1-10 hours, is defined as the ratio between the volume of distillate that is required to re-establish the inlet concentration of the dilute solution and the distillate flow rate produced by the MD module. Notably, t_{RED} = 5h was arbitrarily set in order to have also reasonable operation times on the MD sides: in some conditions high t_{RED} may lead to t_{MD} larger than 12h, thus requiring operator shift during the monitoring of the future proof of concept. The distillate produced in the MD unit is continuously cooled and accumulated in the LOW REG tank where also the RED outlet dilute solution is stored. Conversely, once the MD concentrate reaches the desired concentration, it is discharged in the HIGH IN and a new cycle starts. Finally, for what concerns the temperature of the outlet MD solutions, according to literature data [46], the temperature of the concentrate solution Q_4 is between 5 and 10°C higher than the inlet MD feed, while the distillate Q_D is at a

temperature of around 40°C in the investigated system conditions. Overall, these temperatures are slightly higher than the MD feed temperature, which is equal to the operating temperature of the RED unit. Thus, a cooling unit both for the distillate before the LOW REG tank and for the concentrate before the HIGH REG tank was employed in order to let RED unit to be operated always at ambient temperature. It is well known that RED unit performance can be enhanced by operating it at higher temperature, but including temperature effect in the model would require knowing the dependence of the RED unit (including membrane properties) on temperature via suitable correlations, and this will be matter of future work.

2.1 Hierarchical Model for the RED process

The RED stack (Figure 3) is composed of a certain number of elementary units, called cell pairs, placed one next to the other between two end-electrodes. The latter are connected through an external circuit to an external load [3]. Each cell pair (highlighted in Figure 3) consists of one Anionic Exchange Membrane (AEM), one Cationic Exchange Membrane (CEM), one channel hosting the dilute solution and another channel for the concentrate solution. The channels are typically filled with thin spacers, which separate the membranes thereby providing mechanical stability to the channel and defining its thickness [47]. The concentrate and the dilute solutions are alternatively fed to the channels generated by two adjacent membranes. The concentration gradient is the driving force for the passage of ions, whose path is constrained by the presence of the selective membranes. Thus, a separation of the ions takes place, yielding a flux of anions toward the anode and a flux of cations toward the cathode. The flux of ions is converted into a flux of electrons in the external circuit, through redox reactions. These reactions take place in the electrode compartments, fed by a solution containing a suitable redox couple [36]. The main output electric variables are: the electrical resistance of the stack (R_{stack}), the potential difference generated by the stack at open circuit conditions (Open Circuit Voltage, OCV) and the maximum power density achievable ($P_{d,max}$).

A multi-scale model was developed to predict the behaviour of the RED unit. The lowest scale of the model concerns all the phenomena occurring within the cell-pair, including the fluid dynamics inside the channels taken into account via literature correlations derived from Computational Fluid Dynamics (CFD) simulations. The

higher scale model includes all the *cell pair* models and is relevant to the whole *stack* presented in Figure 3. The developed model for the Reverse Electrodialysis process was implemented in gPROMs Model Builder®, a software suitable for dealing with hierarchical structure models, as the one here proposed [4,48]. Full details of the model along with the membrane properties adopted are reported in the *Supplementary Materials (S1)*.

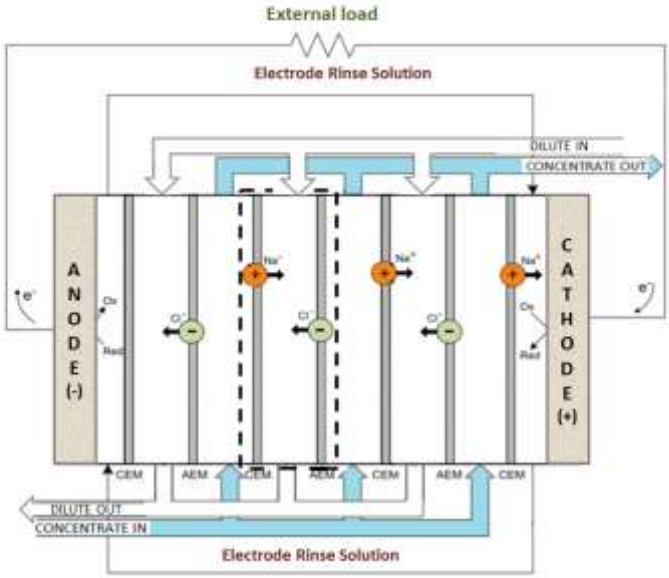

Figure 3. Schematic representation of the RED stack, adapted from ref [48]

2.2 Membrane Distillation (MD): correlations from a validated literature model

The membrane distillation process is a temperature-driven membrane process, in which the separation of the vapour from an aqueous solution takes place through hydrophobic and micro-porous membranes. A sketch is reported in Figure 4.

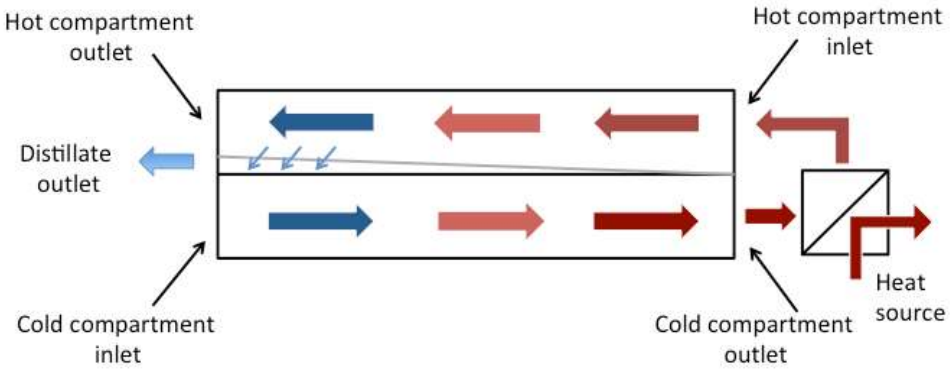

Figure 4. Schematic representation of a MD unit.

Different possible configurations of a MD unit exist: a novel concept of vacuum-assisted air gap module (V-AGMD) configuration developed by Aquastill® was selected for this work.

The module length has a strong impact on the Specific Thermal Consumption (STC), which is defined as the total thermal energy supplied by an external source divided by the permeate produced. Therefore, in the investigated configuration, the feed is firstly sent to the cold compartment and it is preheated by the fluid flowing in the hot compartment. Exiting from the cold compartment, it is heated up to T_{hot} (80°C) through an external source. Thus, the longer the MD unit, the higher the heat recovery from the hot compartment.

In this study, the MD process is described through some correlations, derived from the simulation results kindly supplied by Aquastill® for current commercial modules with channel lengths of 1.5 m and 5 m. These data reported in the *Supplementary Materials (S2.1)*, are collected employing the validated model described extensively in [49]. For each case, given a certain feed flow rate and concentration, the required information regards the distillate flow rate (Q_D) and the Specific Thermal Consumption (STC) of the MD unit. The feed flow rate was set equal to 600 l/h, which is a common flow rate for commercial units, while the feed concentration varies depending on the RED inlet concentrations and operating conditions. The simulation results refer to real commercial units where the driving force of the process is largely affected by the solution concentrations. The higher the solution concentration, the higher the depletion in the vapour pressure difference across the membrane and the lower the water flux, leading to a limitation in the maximum concentration of 3M in the longer unit and 4M for the smaller one.

Moreover, the performance of future MD modules was evaluated using simulation results provided by Aquastill® considering enhanced MD units able (i) to operate in a larger range of concentrations (from 1 to 5M) and (ii) to provide higher water flux. These results are reported in the *Supplementary Materials (S2.2)*.

The calculation of Q_D and STC is performed using the above-mentioned correlations (see eq. S.27). Instead of calculating the figures at the average concentration in the MD unit, the concentration range from the MD feed concentration up to the desired outlet concentration was divided into four intervals. Since Q_D and STC are expressed as functions of the concentration in the feed compartment, it is possible to calculate Q_D

and STC for each concentration interval. Finally, the sum of the products of Q_D and STC for any interval gives the total thermal energy requirement of the MD module.

2.3 RED-MD integration

In order to simulate the performances of the whole system, the RED model was integrated with the MD correlations, according to the system layout shown in Figure 2. Once RED feeding solutions features have been chosen ($C_{high,in}$, $C_{low,in}$, $Q_{high,in}$ and $Q_{low,in}$), RED model is used to calculate $C_{high,out}$, $C_{low,out}$, $Q_{high,out}$ and $Q_{low,out}$. The bypass flow rate Q_{bypass}, (i.e. the fraction of the outlet dilute solution to be mixed with the outlet concentrate one, see Figure 2) is evaluated through a mass balance on the solute:

$$C_{high,out}Q_{high,out} + C_{dil,out}Q_{bypass} = C_{high,in}Q_{high,in} \quad (1)$$

Thus, the stream to be sent to the regeneration section results from the mixing of the outlet concentrate solution and the bypass solution. This solution is accumulated for 5 hours of continuous operation of the RED unit, before being fed to the MD unit: the MD feed solution volume and concentration are indicated hereafter as V_{mix} and C_{mix}. In order to close the loop, the remaining part of the outlet dilute solution has to be mixed with the distillate produced by the MD as indicated by the following balance, which is used to calculate the amount of distillate ($V_{distillate}$):

$$(Q_{low,out} - Q_{bypass}) * 5h + V_{distillate} = Q_{low,in} * 5h \quad (2)$$

As far as the MD is concerned, the distillate flow rate can be easily calculated on the basis of the average solution concentration within the MD unit and the STC is estimated as function of Q_D, according to the correlations reported in the *Supplementary Materials (S2).* The ratio between the required distillate volume ($V_{distillate}$) and the distillate flow rate Q_D corresponds to the working hours of the MD unit. The product of the STC times $V_{distillate}$ gives the total thermal energy consumption, required by the regeneration process. Therefore, the energy efficiency of the cycle η, is given by the ratio between the total net energy which is produced by the RED stack in 5 hours, and the total thermal energy consumption. Together with the energy efficiency, it is possible to calculate the exergy efficiency η_{ex}, as the ratio between the energy efficiency of the cycle η_{en} and the energetic efficiency η_C of a Carnot cycle, which operates at the same temperatures:

$$\eta_{ex} = \frac{\eta_{en}}{\eta_C} \quad (3)$$

This last definition is commonly considered as more appropriate for a comparison among different heat engines [11].

3. Results and discussion

The results section consists of two main parts: one is devoted to describing the performances of an integrated system composed of a real RED and a real MD unit. Conversely, the second part deals with the combination of highly performing equipment. All the simulations were performed fixing some parameters, e.g. RED stack number of cell pairs (equal to 50) and RED membrane width and length (i.e. 0.1 and 0.88 m, respectively), which correspond to the size of a real RED equipment. In all cases, the RED unit is fed by NaCl-water solutions in counter-current arrangement. Concerning the Membrane Distillation unit, the nominal feed flow rate was set equal to 600 l/h in all cases. Regarding the MD geometry, in the real case, the MD unit length depends on the concentration, which has to be reached in the regeneration section. In particular, a maximum concentration of 4M is fixed for the smaller MD unit (1.5m) and of 3M for the longer one (5m). Conversely, in the second case (i.e. enhanced MD units), no limitations were imposed in terms of reachable concentration and a wider range of concentration, up to 5M, was investigated.

3.1 Closed-loop results

For this first case, a parametric study was performed by letting RED inlet concentrations and fluid velocities to vary within a range of typical values and by investigating the two MD unit lengths (i.e. 1.5m and 5m). For what concerns the concentrations of the solutions fed to the RED stack, the concentrate one was supposed to vary from 1M up to 4M, while for the dilute solution the concentration values of 0.01M, 0.05M and 0.1M were taken into account. While varying the concentrations, the fluid velocities were kept fixed and equal to the typical value of 1 cm/s in both compartments. Thus, the most performing set of inlet concentrations and MD unit length was fixed and the fluid velocities were varied from 0.5 cm/s to 2 cm/s for both the dilute and the concentrate compartment. In order to be able to determine the integrated system behaviour, firstly, it is fundamental to know the power density produced in the RED unit and the specific thermal consumption occurring in the MD unit. Finally, the combination of total thermal consumption and net power produced gives rise to the cycle efficiency, which is defined as the ratio of the net energy

produced by the RED unit in 5 hours and the thermal energy required by the MD unit. The exergy efficiency is defined as the ratio of the energetic efficiency and the Carnot efficiency. The latter is equal to 17%, considering T_{cold}=20°C and T_{hot}=80°C. All the results are reported in terms of exergy efficiency, since it is a more straight-forward figure for the comparison with other heat engines. The results relevant to the system performances varying the concentrations and the MD length are reported in Figure 5 and Figure 6. Regarding the $P_{d,net}$ chart, as expected, the producible power density increases when $C_{high,in}$ increases and when $C_{low,in}$ decreases, since these two lead to an enhancement of the available driving force. Therefore, the maximum produced $P_{d,net}$ occurs at $C_{high,in}$ = 4M and $C_{low,in}$ = 0.01M.

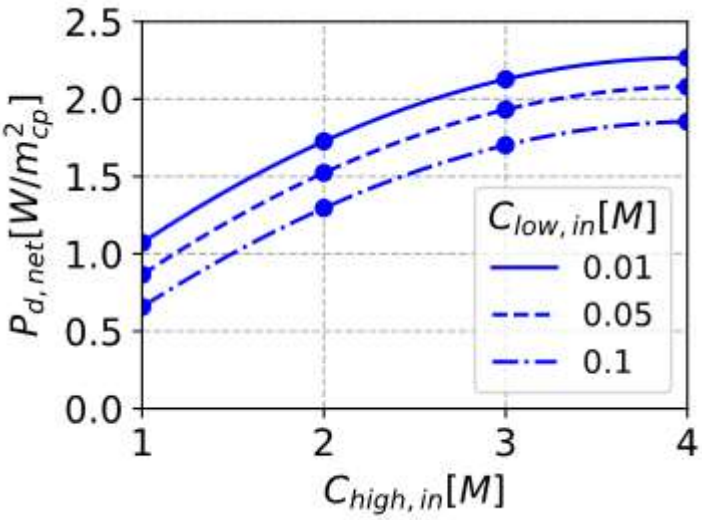

Figure 5. $P_{d,net}$ trend varying the concentrations in the concentrate and in the dilute compartment and the MD unit lenght. (RED stack features: membrane length=0.88 m, N_{cell}=50, counter-current arrangement, t_{RED}=5h, v_{high}=v_{low}=1 cm/s). The dots correspond to the performed simulations and the lines represent the trends.

For what concerns the STC variation, shown in Figure 6 (left), it is possible to observe that the concentration of the dilute solution has a negligible role. Therefore, the trends at $C_{low,in}$=0.01M, 0.05M and 0.1M are almost overlapped. This is not surprising because the role of $C_{high,in}$ in the definition of the MD feed concentration is much more significant. With this respect, it is noticeable that the higher $C_{high,in}$, the higher the STC, since the increase of the concentration corresponds to a reduction of the partial vapour pressure of water at the membrane interface and consequently a depletion of the driving force. This is particularly evident in the trend of the STC relevant to the long module. In this case, a much deeper increase of the thermal consumption takes place, because

the longer module is more affected by the fall of the driving force, since it works at a higher average concentration. For this reason, the longer module cannot operate at concentration higher than 3M.

Finally, the global exergy efficiency of the RED-MD HE, reported in Figure 6 (right), shows the overall performance of the closed loop, as a function of $C_{high,in}$, for the same two MD unit lengths and the same three values of $C_{low,in}$. For the whole range of concentrations, the exergy efficiencies achievable with the longer MD unit are higher than the ones relevant to the shorter unit, because of the different thermal consumption. It is remarkable that both trends relevant to the two MD unit lengths encounters a maximum: the one in blue (L_{MD}=1.5m) has the highest exergy efficiency at $C_{high,in}$=3M while the one in red (L_{MD}=5m) at $C_{high,in}$=2M. Also in this case, this is due to the different STC trends, since the $P_{d,net}$ is the same in the two cases and it increases with $C_{high,in}$. In fact, for the case of the longer MD unit, the net increase of the STC becomes prominent at $C_{high,in}$>2M, thus causing a decreasing trend of the exergy efficiency. Conversely, the flatter trend of the STC relevant to the shorter MD unit ensures an increasing trend of the exergy efficiency up to $C_{high,in}$=3M and also the efficiency reduction after the maximum is much less enhanced than in the case of L_{MD}=5m. Finally, the role of $C_{low,in}$ is more evident for the longer MD unit where the STC is lower. In general, $C_{low,in}$ reduction is beneficial for the engine as the lower $C_{low,in}$, the higher the producible $P_{d,net}$ and the exergy efficiency. Overall, the highest exergy efficiency is reached at $C_{low,in}$=0.01M, $C_{high,in}$=2M and L_{MD}=5m and it corresponds to 2.22%.

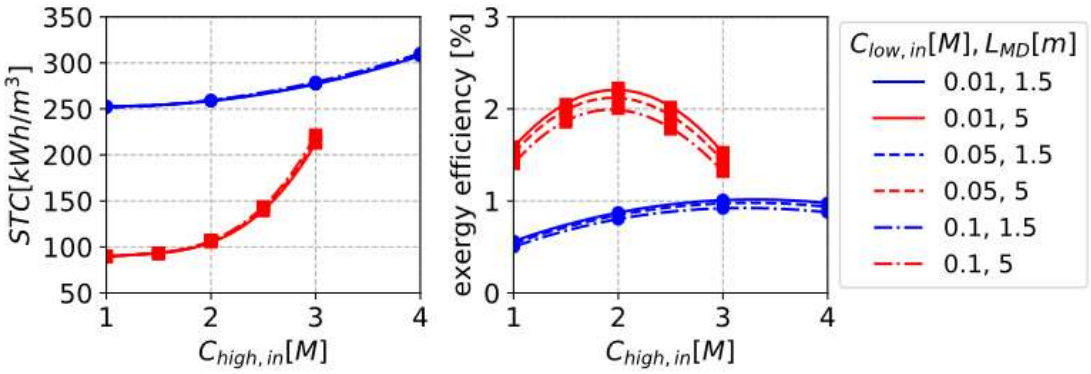

Figure 6. STC (left) and exergy efficiency (right) varying the concentrations in the concentrate and in the dilute compartment and the MD unit lenght. (RED stack features: membrane length=0.88 m, N_{cell}=50, counter-current arrangement, t_{RED}=5h, v_{high}=v_{low}=1 cm/s. MD unit features: T_{hot}=80°C and T_{low}=20°C). The dots correspond to the performed simulations and the lines represent the trends.

Having selected the set of concentrations, which correspond to the maximum exergy efficiency, the following analysis regards the impact of the solution velocities on the RED, MD and whole cycle performances. In particular, Figure 7 shows the trends of $P_{d,net}$ as a function of $v_{low,in}$ and $v_{high,in}$ which are let to vary within the same range. Conversely, Figure 8 reports the corresponding STC and exergy efficiency trends. Regarding the $P_{d,net}$ results, firstly, the role of $v_{low,in}$ is quite significant: an increase of $v_{low,in}$ corresponds to an increase of $P_{d,net}$, since a higher dilute inlet velocity (i.e. a lower residence time) leads to a lower dilute concentration variation along the channel (i.e. an almost constant driving force along the RED stack). For what concerns $v_{high,in}$, its variation commonly leads to a less significant variation of $P_{d,net}$ if compared with the $v_{low,in}$ variation effect.

In general, a maximum is typically observable in these trends due to the competitive effect of (i) non-ohmic resistance reduction (i.e. residence time and polarization resistances) (ii) and pumping power increase. Interestingly, this maximum is not observable for the case of $v_{low,in}$=0.5cm/s as it probably occurs at $v_{high,in}$ lower than the minimum investigated here (i.e. $v_{high,in}$=0.5cm/s).

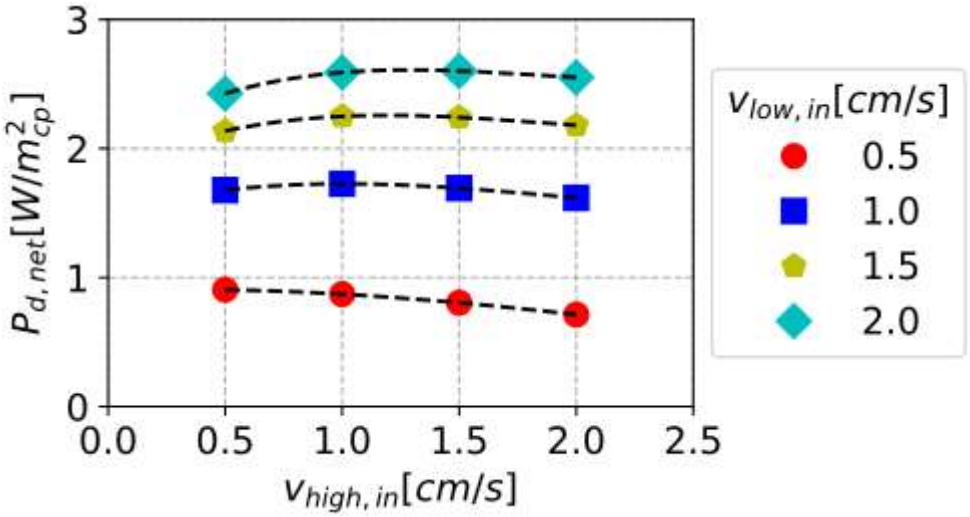

Figure 7. $P_{d,net}$ varying the velocities in the concentrate and in the dilute compartment. (RED stack features: membrane length=0.88 m, N_{cell}=50, counter-current arrangement, t_{RED}=5h, C_{high}= 3M and C_{low}=0.01M). The dots correspond to the performed simulations and the lines represent the trends.

The dependence of the MD unit performance on the velocity of the solution fed to the RED stack is shown in Figure 8, which reports the trends of STC (left) and of the exergy efficiency (right). The STC increases with $v_{high,in}$ at any $v_{low,in}$ and it decreases with the

increase of $v_{low,in}$ (Figure 8-left). The STC value depends on the distillate flow rate produced in the MD unit, which is estimated on the basis of the concentration of the MD feed solution, as reported in the *Supplementary Materials (S2)*. The higher $v_{high,in}$, the higher the outlet concentration of the concentrate solution, which leads to a higher concentration of the MD feed and a lower distillate flow rate. Conversely, the concentration of the MD feed decreases when $v_{low,in}$ increases.

Overall, the combination of the $P_{d,net}$ and STC results gives rise to the exergy efficiency (Figure 8-right), which shows a decreasing trend with $v_{high,in}$ at any $v_{low,in}$, due to the STC increase. Remarkably, the trend of the exergy efficiency at $v_{low,in}$=0.5 cm/s has the highest slope, since $P_{d,net}$ decreases with $v_{high,in}$ in the whole range investigated (see Figure 7). In all cases apart from that of $v_{low,in}$=0.5 cm/s, the exergy efficiency decreases when $v_{low,in}$ increases although $P_{d,net}$ increases and STC decreases. This occurs because the total waste heat requirement depends on the distillate flow rate and on the STC. At higher $v_{low,in}$, the weight of the increase of the distillate flow rate is prominent compared to the STC reduction. Moreover the rise of the waste-heat requirement prevails on the $P_{d,net}$ enhancement, thus resulting into the fore-mentioned exergy efficiency decrease. Finally, the highest exergy efficiency, equal to 2.31%, is achieved in the case of $v_{high,in}$=$v_{low,in}$=0.5 cm/s.

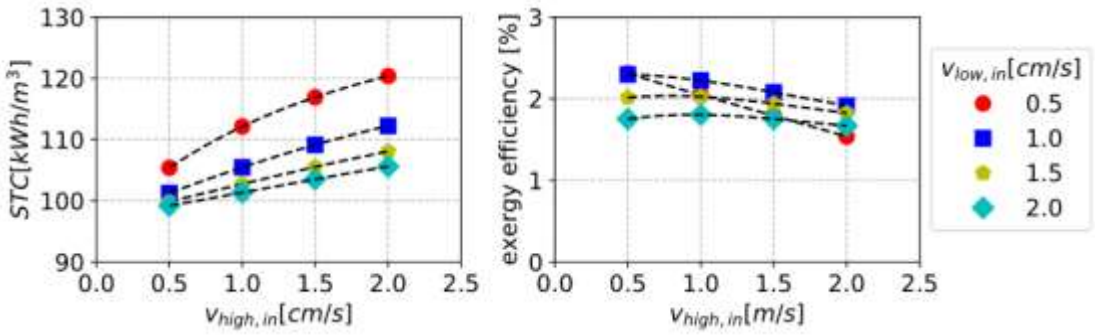

Figure 8. STC (left) and exergy efficiency (right) varying the velocities in the concentrate and in the dilute compartment. (RED stack features: membrane length=0.88 m, N_{cell}=50, counter-current arrangement, t_{RED}=5h, C_{high}= 3M and C_{low}=0.01M. MD unit features: length=5 m, T_{hot}=80°C and T_{low}=20°C). The dots correspond to the performed simulations and the lines represent the trends.

3.2 Closed-loop results with highly-performing RED membranes

A perspective analysis was carried out analysing the effect of using high performing IEMs in the RED unit (membrane properties reported in Table 1) and future MD modules (module performance reported in *Supplementary Materials*, section S2.1) on the efficiency of the cycle. Notably, the input of this scenario should not be considered

as far from reality, rather, these can be reasonably considered as achievable technological targets in the foreseen future.

Table 1. Properties used to simulate RED highly-performing membranes.

Membrane properties	Value
Electrical resistance	Current value*/8
Permselectivity	0.98
Salt diffusivity	Current value**/4
Water permeability	Current value***/4

* Supplementary Materials eq.S4-S5
** 10^{-12} m^2/s [4]
*** 8 ml / (bar h m^2)

As a matter of fact, the RED membrane properties of this scenario were selected by referring to the best values among those already achieved and reported in literature [50]. This can be easily inferred from Figure 9, where the resistance and permselectivity values for both current and highly-performing membranes are shown to be comparable with literature values [50]. Similarly, water permeability and salt diffusivity values are in the range of typical literature values: 10^{-11}-10^{-14} m^2/s for salt diffusivity and 1-20 ml/(bar h m^2) for water permeability (see Figure 4 in [51]).

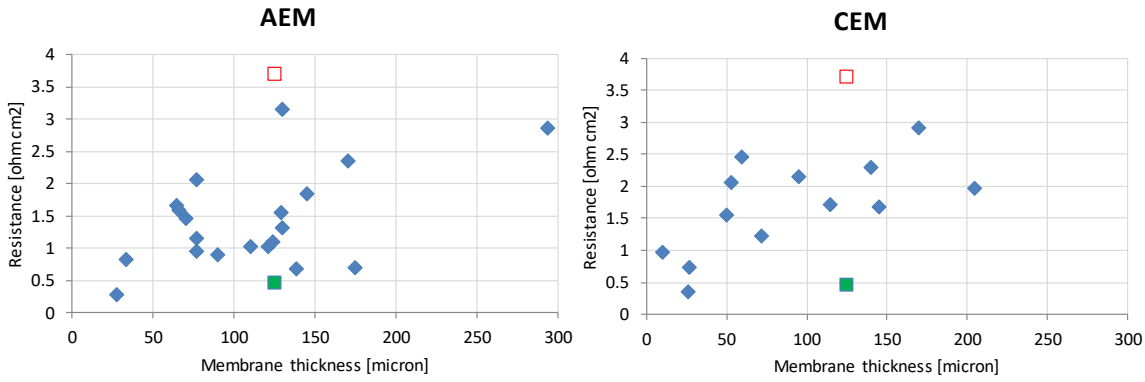

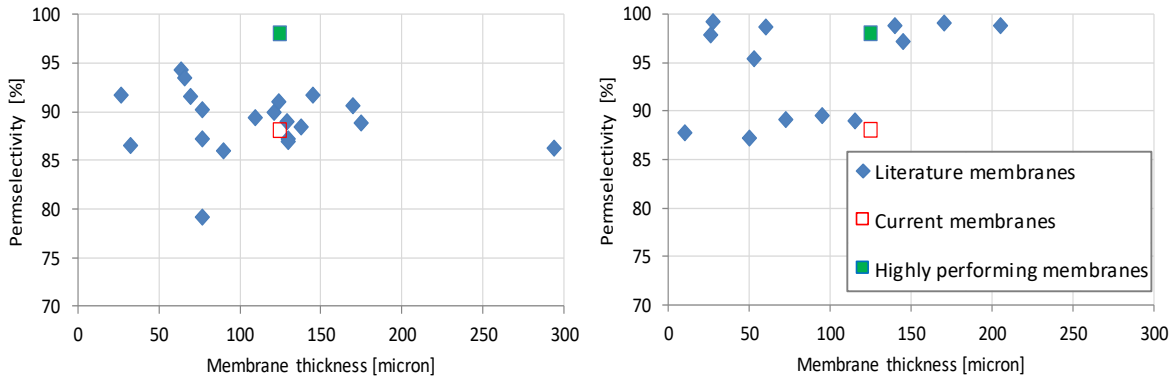

Figure 9: Membrane resistance (up) and permselectivity (down) as a function of membrane thickness for current, literature [50] and highly performing membranes. Left: anionic exchange membranes. Right: cationic exchange membranes. Properties are relevant to measurements at 0.5M for the resistance and 0.5M-0.05M for the permselectivity.

Regarding the MD module, the performances were enhanced accounting for heat recovery improvements and innovative module designs, which are already under development by Aquastill company. We are experimentally characterizing the current Aquastill modules at CIEMAT Plataforma Solar de Almeria for high salinity feeds in v-AGMD performance, and the results so far are consistent with Aquastill calculations [52]. There is certainly room for improvement in Aquastill modules. For instance, the membranes currently used by the company are not designed specifically for the MD process [46]. It has been sufficiently discussed in the literature that optimization of the heat and mass transfer properties of the MD membrane can raise water flux and reduce unit energy consumption [53]. Using a membrane specifically designed for MD, as those currently used in laboratory experiments [32], can give a significant increase in performance, especially for higher salinity. As a matter of fact, the future MD results projected here are similar to current ones at low concentration, and the enhancement is mostly in the high concentration range. Another potential improvement is at the level of module design, for instance using novel spacers for improving heat and mass transfer and reducing the polarization effects between the bulk stream and the membrane surface, which are also more important for high salinity feeds [54–56].

Another possible enhancement of the RED-MD heat engine performance may come from operating the RED unit at higher temperatures, as it is well known that RED unit work well at larger temperatures. However, analysing temperature influence on the cycle performance would require the knowledge of temperature effect on each membrane property and was, thus, not investigated in the present work.

Moreover, also for the case of other SGP engines like the Osmotic Heat Engine, many perspective results relevant to membranes and units able to stand huge pressure difference are usually reported in literature [7,42,43].

In this case, the performance of the system was investigated through sensitivity analyses varying the solutions concentration and velocity. While varying the inlet concentrations, the fluid velocities are kept constant and equal to 0.5 cm/s in both compartments, since this was the most performing set of fluid velocities in the real case. Figure 10 reports the colour-maps relevant to the $P_{d,net}$ and the STC of the engine as a function of $C_{high,in}$ and $C_{low,in}$. As expected, $P_{d,net}$ increases with $C_{high,in}$ in the whole range of investigated concentrations, because of the enhancement of the available driving force in the RED stack. Conversely, $C_{low,in}$ has a minor role in the definition of $P_{d,net}$. This is explicable because a significant variation in the concentration of the fed solutions occurs when long residence times are considered (i.e. long channels and/or low flow rates). In particular, the stream-wise increase of C_{low} along the dilute channel of the RED stack (e.g. from 0.01 M→0.3 M) leads to a reduction of its influence on the produced $P_{d,net}$. Regarding the STC colour-map, as already observed in the first case with current equipment, the concentration of the MD feed depends much more heavily on $C_{high,in}$ and, as a consequence, the variation of the STC with $C_{low,in}$ is almost negligible.

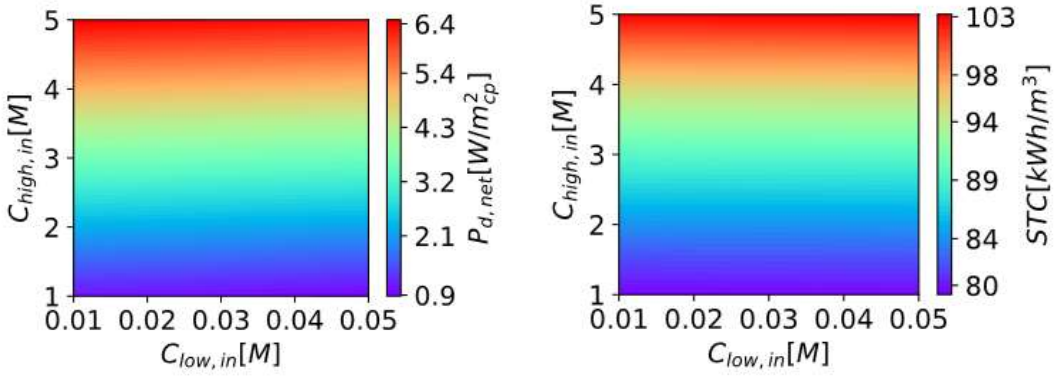

Figure 10. Maps showing the $P_{d,net}$ (left) and the STC (right) varying the concentrations in the concentrate and in the dilute compartment for highly-performing RED membranes. (RED stack features: membrane length=0.88 m, N_{cell}=50, counter-current arrangement, t_{RED}=5h, v_{high}=v_{low}=0.5 cm/s. MD unit features: length=5 m, T_{hot}=80°C and T_{low}=20°C).

Overall, one can observe that using highly-performing RED membranes the effect of the uncontrolled mixing process is reduced, while the migrative flux increases, resulting

in a net increase of the power produced. On the other hand, future MD modules require lower STC than current modules and are able to operate with a wider range of feed concentrations (i.e. up to 5M). For these reasons, the exergy efficiency of the system, reported in the colour-map in Figure 11, presents much higher values, with a maximum of 16.5% at $C_{high,in}$=5M and $C_{low,in}$=0.01M.

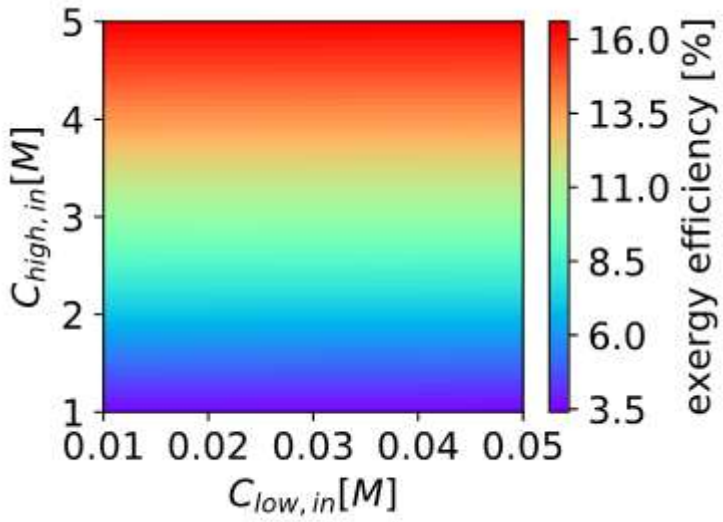

Figure 11. Map showing the exergy efficiency varying the concentrations in the concentrate and in the dilute compartment for highly-performing RED membranes. (RED stack features: membrane length=0.88 m, N_{cell}=50, counter-current arrangement, t_{RED}=5h, v_{high}=v_{low}=0.5 cm/s. MD unit features: length=5 m, T_{hot}=80°C and T_{low}=20°C).

Finally, also in this case the impact of the fluid velocity was investigated taking into account the values of concentrations, which maximized the cycle exergy efficiency (i.e. 5M for the concentrate and 0.01M for the dilute). In Figure 12 the colour-maps relevant to the $P_{d,net}$ and the STC versus the fluid velocities are reported. Differently from what observed varying the solutions concentration, both solution velocities have an appreciable influence on the system performance. Regarding the $P_{d,net}$, a considerable increase of the produced power density is observed when both velocities are maximized. Therefore, in the case of $v_{low,in}$=$v_{high,in}$=1.5 cm/s the $P_{d,net}$ value is doubled with respect to the maximum value observed in Figure 10. Conversely, in order to minimize the STC, the most suitable velocity set presents the minimum investigated $v_{high,in}$ (0.25cm/s) and the maximum investigated $v_{low,in}$ (1.5cm/s). This is explicable because, in this condition, the concentration change in the concentrate solution is maximized, which leads to a lower concentration in the MD feed.

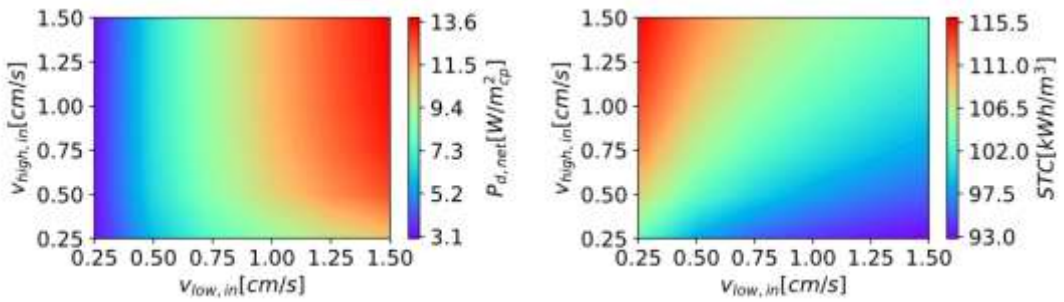

Figure 12. Maps showing the $P_{d,net}$ (left) and STC (right) varying the velocities in the concentrate and in the dilute compartment with highly-performing RED membranes. (RED stack features: membrane length=0.88 m, N_{cell}=50, counter-current arrangement, t_{RED}=5h, C_{high}= 5M and C_{low}=0.01M. MD unit features: length=5 m, T_{hot}=80°C and T_{low}=20°C).

Finally, the map reporting the exergy efficiency values varying the fluid velocities is shown in Figure 13. The combination of the producible power and the thermal consumption gives rise to a maximum of exergy efficiency which is located at $v_{high,in}$=$v_{low,in}$=0.5cm/s, i.e. the same set of velocities employed for the solution concentration analysis. Then, the maximum exergy efficiency achievable with highly performing RED and MD equipment is equal to 16.5%, as already stated. This corresponds to a discontinuous operation where t_{RED}=5h and t_{MD}=1.5h.

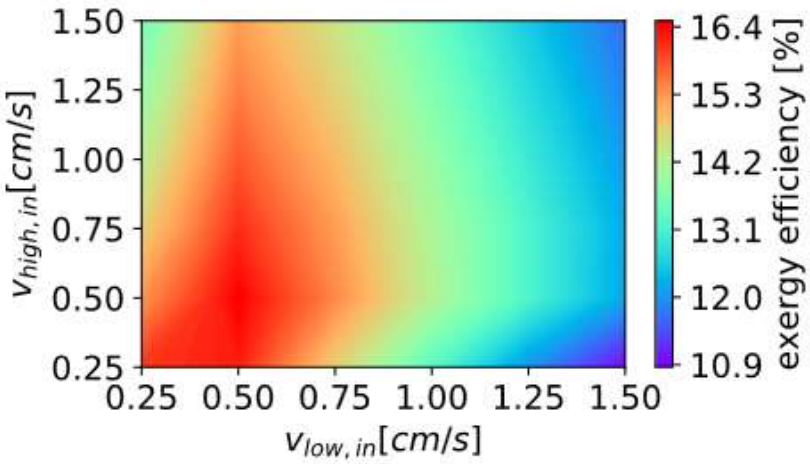

Figure 13. Map showing the exergy efficiency varying the velocities in the concentrate and in the dilute compartment with highly-performing RED membranes. (RED stack features: membrane length=0.88 m, N_{cell}=50, counter-current arrangement, t_{RED}=5h, C_{high}= 5M and C_{low}=0.01M. MD unit features: length=5 m, T_{hot}=80°C and T_{low}=20°C).

3.3 Economic analysis

The economic analysis of the RED-MD unit is based on the calculation of the Levelized Cost Of Electricity (LCOE), which provides a reliable way of estimating the potential of various power production technologies [57]. The LCOE is calculated from Eq. (4).

$$LCOE = \frac{\sum_{t=0}^{n} \frac{I_t + M_t}{(1+r)^t}}{\sum_{t=0}^{n} \frac{E_t}{(1+r)^t}} \quad (4)$$

where t refers to the year "t" with t=0 representing the start of the plant construction (it is considered that this construction requires one whole year), n the plant lifetime, I_t the investment expenditures (capital costs) in the year "t", M_t the running costs (fixed and variable) in the year "t", r the discount rate, and E_t the electricity generation (in kWh) in the year "t", calculated according to the capacity factor and the net power production. The parameters considered for the cost analysis and included in Eq. (4) are given in Table 2, according to estimated financial conditions for discount rate and cost factors of power plants. A capacity factor of 90% was considered in the calculation of the power output from the RED unit.

Parameter	Value
Capacity factor	90%
Plant lifetime (t)	30 years
Discount rate (r)	5%
Other project costs	0.5%/investment
Civil and electrical infrastructure cost [58]	250 €/kW
RED membranes lifetime	10 years
RED membrane specific cost (variable) [59]	1-30 €/m^2
MD module specific cost (variable)	5-120 €/m^2

Table 2. Financial parameters

The operating costs are estimated as a function of the net power production, while maintenance costs mainly include the RED membranes replacement (labour and materials). The sum of these three costs is considered as the OPEX of the plant.

For an average RED membrane and MD module specific costs, the higher capital cost (CAPEX) contribution derives from the RED stacks and the MD unit. In particular, the

MD represents about the 81% of the total capital cost, the 18% of the RED stacks, and the rest to other costs [59].

Variable RED membrane and MD unit specific costs are introduced in the calculations (see Table 2), in order to identify the cost ranges, which can make this technology financially sustainable. These ranges have been greatly expanded, in order to identify the targeted future specific costs that would make this technology financially viable.

According to the methodology presented previously, LCOE values are evaluated for a power plant with net power production of 1 MW, considering the adoption of highly performing ion exchange membranes. Operating conditions were taken from the best case of Figure 13 (i.e. those providing η_{ex}=16.5%), but each RED unit was considered as composed by 162 cell pairs in order to have an operating time for the RED unit equal to that of the MD unit (i.e. $t_{RED}=t_{MD}$), thus guaranteeing a continuous operation of the heat engine.

The LCOE as a function of the RED membrane and MD specific costs is presented in Figure 14.

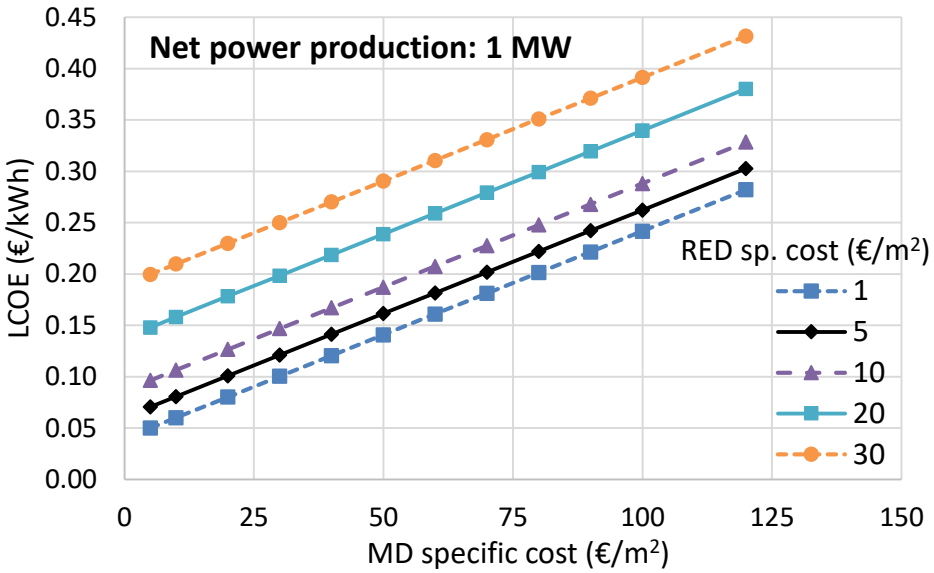

Figure 14. LCOE as function of the RED membrane and MD specific costs of a RED-MD unit with net power production of 1 MW.

It becomes clear that for the RED-MD technology to become cost-effective, the RED membrane specific cost should be reduced to less than 10 €/m^2, accompanied by a strong reduction of the MD specific cost to less than 25 €/m^2. The MD specific cost has the larger effect on the LCOE, since the cost contribution of the MD on the total capital cost is more than 80%.

Currently, the MD specific cost is about 100 €/m^2, while the RED membrane specific cost is about 30 €/m^2. With these costs, the LCOE is almost 0.40 €/kWh, showing that this technology is not ready yet to be deployed at a commercial level. However, both specific costs are declining fast, and combined with the continuing increase of electricity prices, can make the RED-MD technology financially sustainable for heat to power applications.

Conclusions and future perspectives

In this work, an integrated RED-MD system is investigated by carrying out modelling activities. For the first time, a multi-scale model for Reverse Electrodialysis units has been coupled with correlations derived from a model describing a commercial MD unit along with suitable mass and energy balances. The aim of the work was that of identifying the operating conditions and the process configurations maximizing the cycle efficiency in order to drive the design of the first RED-MD heat engine prototype within the EU project RED-Heat-to-Power. Moreover, the system performances were investigated also accounting for highly performing equipment, in order to evaluate the perspectives and the room for improvements of the closed loop.

As concerns the real system, the coupling of a RED unit, fed by a concentrate NaCl-water solution at $C_{high,in}$=2M and $v_{high,in}$=0.5 cm/s and by a dilute solution at $C_{low,in}$=0.01M and $v_{high,in}$=0.5 cm/s, coupled with a long MD unit (L_{MD}=5m) provides the best performance. For this case, exergy efficiency equal to 2.3% was achieved. Higher values can be obtained with improved IEMs and MD unit: with this aim, the IEMs permselectivity was increased and the electrical resistance, water permeability and salt diffusivity were reduced, while, concerning the MD unit, a higher distillate flow rate and a lower STC was assumed. This highly performing system resulted into an exergy efficiency of about 16.5% (corresponding to an energetic efficiency of 2.8%), which is much higher than the values reported in literature until now, yet being still far from the thermodynamic Carnot limit (i.e. energetic efficiency of 17%).

In general, the results show that the high thermal consumption, typical of the current commercial MD unit, causes an overall low conversion efficiency of the RED-MD integrated system. Nevertheless, this technology is still far from being optimized and consolidated, as demonstrated by the large number of research works devoted to improving it. In fact, the forecasted improvements of the MD performances lead to a

drastic enhancement of the overall performances. Moreover, the simplicity of the coupling scheme and the ease of scalability make this coupling choice interesting in general and particularly suitable for the implementation at the laboratory scale. Finally, an economic analysis showed that the expectable future reduction of the specific costs of the RED and the MD equipment, together with the possibility to use low-grade waste heat, may make the RED-MD coupling a promising and economically competitive heat to power technology.

Acknowledgements

This work was performed within the RED-Heat-to-Power project (Conversion of Low Grade Heat to Power through closed loop Reverse Electro-Dialysis) - Horizon 2020 programme, Project Number: 640667: www.red-heat-to-power.eu.

Nomenclature

A	membrane area [m^2]
a_w	water activity [-]
b	membrane width [m]
C	solution molarity [mol/m^3]
A_Φ, α , b	Pitzer's model constants [$(kg/mol)^{1/2}$]
f_γ, B_γ, C^γ, B^Φ	Pitzer's model coefficients [-]
A_Λ, B_Λ, C_Λ	coefficients of Jones and Dole's equation
D	salt diffusivity in solution [m^2/s]
D^{membr}	salt diffusivity through the membrane [m^2/s]
ΔP	distributed pressure drops [Pa]
E	voltage [V]
f	friction coefficient [-]
i	current [A]
J	molar flux [$mol/(m^2\ s)$]
J'	volumetric flux [m/s]
m	solution molality [mol/kg]
M_w	molecular weight [g/mol]
N_{cell}	number of cell pairs [-]
N	number of discretized elements [-]
P_d	power density [W/m^2]
Q	volume flow rate [m^3/s]
R	universal gas constant (8.314 J/(mol K))
$R_{channel}$	channel resistance [Ω]
R_{blank}	blank resistance [$\Omega\ m^2$]
R_{IEM}	electrical resistance of ionic exchange membrane [Ω]
R_{cell}	cell pair electrical resistance [Ω]
R_{ext}	electrical resistance of the external load [Ω]
Re	Reynolds number [-]
Sh	Sherwood number [-]
s_f	shadow factor [-]
t_{RED}	working time of the RED unit [h]
t_{MD}	working time of the MD unit [h]
T	temperature [°C]
v	fluid velocity [m/s]

Greek letters

α	permselectivity [-]
$\beta^{(0)}$, $\beta^{(1)}$, C^Φ	Pitzer's model parameters defined for the salt-water solution [-]
γ	salt activity coefficient [-]
δ	spacer thickness [m]
η	energy efficiency [%]
η_c	Carnot efficiency [%]
η_{ex}	exergy efficiency [%]
θ	polarization coefficient [-]
Λ_0	salt equivalent conductivity at infinite dilution [mS l/(cm mol)]
Λ	salt equivalent conductivity [mS l/(cm mol)]
ρ	solution mass density [kg/m^3]
φ	osmotic coefficient [-]

Subscripts

high	concentrate compartment
low	dilute compartment
high,in	inlet concentrate solution
low,in	inlet dilute solution
cell	cell pair
stack	stack
AEM	anion exchange membrane
CEM	cation exchange membrane
net	power density minus the pumping losses

Acronyms

IEM	Ion Exchange Membrane
MD	Membrane Distillation
MED	Multi-Effect Distillation
OCV	Open Circuit Voltage
PRO	Pressure Retarded Osmosis
RED	Reverse Electrodialysis
REDHE	Reverse Electrodialysis Heat Engine
SGP	Salinity Gradient Power
STC	Specific Thermal Consumption

References

[1] A. Achilli, T.Y. Cath, A.E. Childress, Power generation with pressure retarded osmosis: An experimental and theoretical investigation, J. Memb. Sci. 343 (2009) 42–52. doi:10.1016/j.memsci.2009.07.006.

[2] S. Loeb, Large-scale power production by pressure-retarded osmosis, using river water and sea water passing through spiral modules, Desalination. 143 (2002) 115–122.

[3] D.A. Vermaas, E. Guler, M. Saakes, K. Nijmeijer, Theoretical power density from salinity gradients using reverse electrodialysis, Energy Procedia. 20 (2012) 170–184. doi:10.1016/j.egypro.2012.03.018.

[4] M. Tedesco, A. Cipollina, A. Tamburini, I.D.L. Bogle, G. Micale, A simulation tool for analysis and design of reverse electrodialysis using concentrated brines, Chem. Eng. Res. Des. 93 (2015) 441–456. doi:10.1016/j.cherd.2014.05.009.

[5] J.W. Post, C.H. Goeting, J. Valk, S. Goinga, J. Veerman, H.V.M. Hamelers, P.J.F.M. Hack, Towards implementation of reverse electrodialysis for power generation from salinity gradients power generation from salinity gradients, Desalin. Water Treat. 16 (2010) 182–193. doi:10.5004/dwt.2010.1093.

[6] J.W. Post, J. Veerman, H.V.M. Hamelers, G.J.W. Euverink, S.J. Metz, K. Nymeijer, C.J.N. Buisman, Salinity-gradient power: Evaluation of pressure-retarded osmosis and reverse electrodialysis, J. Memb. Sci. 288 (2007) 218–230. doi:10.1016/j.memsci.2006.11.018.

[7] B.E. Logan, M. Elimelech, U. States, Membrane-based processes for sustainable power generation using water, Nature. 488 (2012) 313–319. doi:10.1038/nature11477.

[8] N.Y. Yip, M. Elimelech, Comparison of Energy Efficiency and Power Density in Pressure Retarded Osmosis and Reverse Electrodialysis, Environ. Sci. Technol. 48 (2014) 11002–11012.

[9] A. Daniilidis, D.A. Vermaas, R. Herber, K. Nijmeijer, Experimentally obtainable energy from mixing river water, seawater or brines with reverse electrodialysis, Renew. Energy. 64 (2014) 123–131. doi:10.1016/j.renene.2013.11.001.

[10] M. Tedesco, A. Cipollina, A. Tamburini, G. Micale, J. Helsen, M. Papapetrou, REAPower: use of desalination brine for power production through reverse electrodialysis, Desalin. Water Treat.

53 (2014) 3161–3169. doi:10.1080/19443994.2014.934102.
[11] A. Tamburini, A. Cipollina, M. Papapetrou, A. Piacentino, G. Micale, Salinity gradient engines, in: Sustain. Energy from Salin. Gradient, 2016: p. 219–256 (Chapter 7).
[12] M. Papapetrou, G. Kosmadakis, A. Cipollina, U. La Commare, G. Micale, Industrial waste heat: Estimation of the technically available resource in the EU per industrial sector, temperature level and country, Appl. Therm. Eng. 138 (2018) 207–216. doi:10.1016/j.applthermaleng.2018.04.043.
[13] Conversion of Low Grade Heat to Power through closed loop Reverse ElectroDialysis—Horizon 2020 programme, Project Number: 640667: www.red-heat-to-power.eu, (n.d.).
[14] A. Tamburini, M. Tedesco, A. Cipollina, G. Micale, M. Ciofalo, M. Papapetrou, W. Van Baak, A. Piacentino, Reverse electrodialysis heat engine for sustainable power production, Appl. Energy. (2017).
[15] A. Cipollina, G. Micale, L. Rizzuti, Seawater Desalination, 2006. doi:10.2174/97816080528511060101.
[16] B. Ortega-Delgado, P. Palenzuela, D.-C. Alarcon-Padilla, Parametric study of a multi-effect distillation plant with thermal vapor compression for its integration into a Rankine cycle power block, Desalination. 394 (2016) 18–29. doi:10.1016/j.desal.2016.04.020.
[17] A. Cipollina, M.G. Di Sparti, A. Tamburini, G. Micale, Development of a Membrane Distillation module for solar energy seawater desalination, Chem. Eng. Res. Des. 90 (2012) 2101–2121. doi:10.1016/j.cherd.2012.05.021.
[18] A. Alkhudhiri, N. Darwish, N. Hilal, Membrane distillation: A comprehensive review, Desalination. 287 (2012) 2–18. doi:10.1016/j.desal.2011.08.027.
[19] L.M. Camacho, L. Dumée, J. Zhang, J. Li, M. Duke, Advances in Membrane Distillation for Water Desalination and Purification Applications, Water. 5 (2013) 94–196. doi:10.3390/w5010094.
[20] M.L. Stone, C. Rae, F.F. Stewart, A.D. Wilson, Switchable polarity solvents as draw solutes for forward osmosis, Desalination. 312 (2013) 124–129. doi:10.1016/j.desal.2012.07.034.
[21] S.M. Mercer, P.G. Jessop, "Switchable Water": Aqueous Solutions of Switchable Ionic Strength, ChemSusChem. 3 (2010) 467–470. doi:10.1002/cssc.201000001.
[22] X. Luo, X. Cao, Y. Mo, K. Xiao, X. Zhang, P. Liang, X. Huang, Power generation by coupling reverse electrodialysis and ammonium bicarbonate : Implication for recovery of waste heat, Electrochem. Commun. 19 (2012) 25–28. doi:10.1016/j.elecom.2012.03.004.
[23] M. Bevacqua, A. Carubia, A. Cipollina, A. Tamburini, M. Tedesco, G. Micale, Performance of a RED system with ammonium hydrogen carbonate solutions, Desalin. Water Treat. 57 (2016) 23007–23018. doi:10.1080/19443994.2015.1126410.
[24] X. Zhu, W. He, B.E. Logan, Influence of solution concentration and salt types on the performance of reverse electrodialysis cells, J. Memb. Sci. 494 (2015) 154–160. doi:10.1016/j.memsci.2015.07.053.
[25] A. Bevacqua, M., Tamburini, A., Papapetrou, M., Cipollina, A., Micale, G., Piacentino, Reverse electrodialysis with NH4HCO3-water systems for heat-to-power conversion, Energy. (2017). doi:doi:10.1016/j.energy.2017.07.012.
[26] S. Al-Obaidani, E. Curcio, F. Macedonio, G. Di Profio, H. Al-Hinai, E. Drioli, Potential of membrane distillation in seawater desalination: Thermal efficiency, sensitivity study and cost estimation, J. Memb. Sci. 323 (2008) 85–98. doi:10.1016/j.memsci.2008.06.006.
[27] N. Ghaffour, J. Bundschuh, H. Mahmoudi, M.F.A. Goosen, Renewable energy-driven desalination technologies: A comprehensive review on challenges and potential applications of integrated systems, Desalination. 356 (2015) 94–114. doi:10.1016/j.desal.2014.10.024.
[28] G. Ruiz-Aguirre, A., Andres-Mañas J.A., Fernández-Sevilla J.M., Zaragoza, Comparative characterization of three commercial spiral-wound membrane distillation modules., Desalin. Water Treat. 61 (2017) 152–159.
[29] N. Ghaffour, T.M. Missimer, G.L. Amy, Technical review and evaluation of the economics of water desalination: Current and future challenges for better water supply sustainability, Desalination. 309 (2013) 197–207. doi:10.1016/j.desal.2012.10.015.
[30] U.K. Kesieme, N. Milne, H. Aral, C. Yong, M. Duke, Economic analysis of desalination technologies in the context of carbon pricing, and opportunities for membrane distillation, Desalination. 323 (2013) 66–74. doi:10.1016/j.desal.2013.03.033.
[31] F. Laganà, G. Barbieri, E. Drioli, Direct contact membrane distillation: modelling and concentration experiments, J. Memb. Sci. 166 (2000) 1–11.
[32] M. Khayet, Membranes and theoretical modeling of membrane distillation: A review, Adv. Colloid Interface Sci. 164 (2011) 56–88. doi:10.1016/j.cis.2010.09.005.
[33] P. Długołęcki, A. Gambier, K. Nijmeijer, M. Wessling, Practical potential of reverse

electrodialysis as process for sustainable energy generation, Environ. Sci. Technol. 43 (2009) 6888–6894. doi:10.1021/es9009635.
[34] M. Tedesco, C. Scalici, D. Vaccari, A. Cipollina, A. Tamburini, G. Micale, Performance of the first reverse electrodialysis pilot plant for power production from saline waters and concentrated brines, J. Memb. Sci. 500 (2016) 33–45. doi:10.1016/j.memsci.2015.10.057.
[35] L. Gurreri, A. Tamburini, A. Cipollina, G. Micale, CFD analysis of the fluid flow behavior in a reverse electrodialysis stack, Desalin. Water Treat. 48 (2012) 390–403. doi:10.1080/19443994.2012.705966.
[36] O. Scialdone, C. Guarisco, S. Grispo, A.D. Angelo, A. Galia, Investigation of electrode material – Redox couple systems for reverse electrodialysis processes. Part I: Iron redox couples, J. Electroanal. Chem. 681 (2012) 66–75. doi:10.1016/j.jelechem.2012.05.017.
[37] P. Długołecki, P. Ogonowski, S.J. Metz, M. Saakes, K. Nijmeijer, M. Wessling, On the resistances of membrane , diffusion boundary layer and double layer in ion exchange membrane transport, J. Memb. Sci. 349 (2010) 369–379. doi:10.1016/j.memsci.2009.11.069.
[38] A.B. Yaroslavtsev, V. V. Nikonenko, Ion-exchange membrane materials: Properties, modification, and practical application, Nanotechnologies Russ. 4 (2009) 137–159. doi:10.1134/S199507800903001X.
[39] N.P. Berezina, N.A. Kononenko, O.A. Dyomina, N.P. Gnusin, Characterization of ion-exchange membrane materials: Properties vs structure, Adv. Colloid Interface Sci. 139 (2008) 3–28. doi:10.1016/j.cis.2008.01.002.
[40] H.J. Cassady, E.C. Cimino, M. Kumar, M.A. Hickner, Specific ion effects on the permselectivity of sulfonated poly(ether sulfone) cation exchange membranes, J. Memb. Sci. 508 (2016) 146–152. doi:10.1016/j.memsci.2016.02.048.
[41] G.M. Geise, H.J. Cassady, D.R. Paul, B.E. Logan, M.A. Hickner, E. Logan, M.A. Hickner, Specific ion effects on membrane potential and the permselectivity of ion exchange membranes, Phys. Chem. Chem. Phys. 16 (2014) 21673–21681. doi:10.1039/C4CP03076A.
[42] S. Lin, N.Y. Yip, T.Y. Cath, C.O. Osuji, M. Elimelech, Hybrid Pressure Retarded Osmosis−Membrane Distillation System for Power Generation from Low-Grade Heat: Thermodynamic Analysis and Energy Efficiency, Environ. Sci. Technol. 48 (2014) 5306–5313.
[43] E. Shaulsky, C. Boo, S. Lin, M. Elimelech, Membrane-Based Osmotic Heat Engine with Organic Solvent for Enhanced Power Generation from Low-Grade Heat, Environ. Sci. Technol. 49 (2015) 5820–5827. doi:10.1021/es506347j.
[44] R. Long, B. Li, Z. Liu, W. Liu, Hybrid membrane distillation-reverse electrodialysis electricity generation system to harvest low-grade thermal energy, J. Memb. Sci. 525 (2017) 107–115. doi:10.1016/j.memsci.2016.10.035.
[45] R. Ashu, E. Curcio, E. Brauns, W. Van Baak, E. Fontananova, G. Di, Membrane Distillation and Reverse Electrodialysis for Near-Zero Liquid Discharge and low energy seawater desalination, J. Memb. Sci. 496 (2015) 325–333. doi:10.1016/j.memsci.2015.09.008.
[46] A. Ruiz-Aguirre, J.A. Andrés-Mañas, J.M. Fernández-Sevilla, G. Zaragoza, Experimental characterization and optimization of multi-channel spiral wound air gap membrane distillation modules for seawater desalination, Sep. Purif. Technol. 205 (2018) 212–222. doi:10.1016/j.seppur.2018.05.044.
[47] L. Gurreri, A. Tamburini, A. Cipollina, G. Micale, M. Ciofalo, Flow and mass transfer in spacer-filled channels for reverse electrodialysis: a CFD parametrical study, J. Memb. Sci. 497 (2016) 300–317. doi:10.1016/j.memsci.2015.09.006.
[48] M. Tedesco, A. Cipollina, A. Tamburini, W. van Baak, G. Micale, Modelling the Reverse ElectroDialysis process with seawater and concentrated brines, Desalin. Water Treat. 49 (2012) 404–424. doi:10.1080/19443994.2012.699355.
[49] M. Bindels, N. Brand, B. Nelemans, Modeling of semibatch air gap membrane distillation, Desalination. 430 (2018) 98–106. doi:10.1016/j.desal.2017.12.036.
[50] R.A. Tufa, S. Pawlowski, J. Veerman, K. Bouzek, E. Fontananova, G. Di Profio, S. Velizarov, J.G. Crespo, K. Nijmeijer, E. Curcio, Progress and prospects in reverse electrodialysis for salinity gradient energy conversion and storage, Appl. Energy. 225 (2018) 290–331.
[51] R.S. Kingsbury, S. Zhu, S. Flotron, O. Coronell, Microstructure determines water and salt permeation in commercial ion exchange membranes, ChemRxiv. (2018) 1–36. doi:10.26434/chemrxiv.6987248.
[52] J.A. Andrés-Mañas, F.G. Acién, G. Zaragoza, Performance evaluation of a novel vacuum-enhanced air-gap membrane distillation module for regeneration of salinity gradients, in: Desalin. Environ. Clean Water Energy, 2018.
[53] M.I. Ali, E.K. Summers, H.A. Arafat, J.H. Lienhard V, Effects of membrane properties on water production cost in small scale membrane distillation systems, Desalination. 306 (2012) 60–71.

doi:10.1016/j.desal.2012.07.043.
[54] P. Yazgan-Birgi, M.I. Hassan Ali, J. Swaminathan, J.H. Lienhard, H.A. Arafat, Computational fluid dynamics modeling for performance assessment of permeate gap membrane distillation, J. Memb. Sci. 568 (2018) 55–66. doi:10.1016/j.memsci.2018.09.061.
[55] Y.D. Kim, L. Francis, J.G. Lee, M.G. Ham, N. Ghaffour, Effect of non-woven net spacer on a direct contact membrane distillation performance: Experimental and theoretical studies, J. Memb. Sci. 564 (2018) 193–203. doi:10.1016/j.memsci.2018.07.019.
[56] A. Tamburini, M. Renda, A. Cipollina, G. Micale, M. Ciofalo, Investigation of heat transfer in spacer-filled channels by experiments and direct numerical simulations, Int. J. Heat Mass Transf. 93 (2016) 1190–1205. doi:10.1016/j.ijheatmasstransfer.2015.11.034.
[57] M. Papapetrou, A. Cipollina, U. La Commare, G. Micale, G. Zaragoza, G. Kosmadakis, Assessment of methodologies and data used to calculate desalination costs, Desalination. 419 (2017) 8–19. doi:10.1016/j.desal.2017.05.038.
[58] I. Statistics, Capital Cost Estimates for Utility Scale Electricity Generating Plants, 2016.
[59] F. Giacalone, G. Kosmadakis, M. Papapetrou, A. Tamburini, A. Cipollina, G. Micale, Potential of Reverse Electrodialysis in real environments, in: 13th Conf. Sustain. Dev. Energy, Water Environ. Syst. (SDEWES 2018) Palermo, Italy, 2018.
[60] F. Giacalone, P. Catrini, A. Tamburini, A. Cipollina, A. Piacentino, G. Micale, Exergy analysis of reverse electrodialysis, Energy Convers. Manag. 164 (2018) 588–602. doi:10.1016/j.enconman.2018.03.014.
[61] K.S. Pitzer, Thermodynamics of Electrolytes. I. Theoretical Basis and General Equations, J. Phys. Chem. 77 (1973) 268–277. doi:10.1021/j100621a026.
[62] G. Jones, C.F. Bickford, The Conductance of Aqueous Solutions as a Function of the Concentration. I. Potassium Bromide and Lanthanum Chloride, J. Am. Chem. Soc. 56 (1934) 602–611.
[63] M. Micari, M. Bevacqua, A. Cipollina, A. Tamburini, W. Van Baak, T. Putts, G. Micale, Effect of different aqueous solutions of pure salts and salt mixtures in reverse electrodialysis systems for closed-loop applications, J. Memb. Sci. 551 (2018) 315–325. doi:10.1016/j.memsci.2018.01.036.
[64] N. Lakshminarayanaiah, Transport phenomena in artificial membranes, Chem. Rev. 65 (1965) 491–565. doi:10.1021/cr60237a001.
[65] M. La Cerva, M. Di Liberto, L. Gurreri, A. Tamburini, A. Cipollina, G. Micale, M. Ciofalo, Coupling CFD with a one-dimensional model to predict the performance of reverse electrodialysis stacks, J. Memb. Sci. 541 (2017) 595–610. doi:10.1016/j.memsci.2017.07.030.
[66] L. Gurreri, A. Tamburini, A. Cipollina, G. Micale, M. Ciofalo, CFD prediction of concentration polarization phenomena in spacer- filled channels for reverse electrodialysis, J. Memb. Sci. 468 (2014) 133–148. doi:10.1016/j.memsci.2014.05.058.
[67] J. Veerman, M. Saakes, S.J. Metz, H. G.J., Reverse electrodialysis: A validated process model for design and optimization, Chem. Eng. J. 166 (2011) 256–268. doi:10.1016/j.cej.2010.10.071.
[68] E. Güler, W. van Baak, M. Saakes, K. Nijmeijer, Monovalent-ion-selective membranes for reverse electrodialysis, J. Memb. Sci. 455 (2014) 254–270. doi:10.1016/j.memsci.2013.12.054.
[69] L. Gurreri, A. Tamburini, A. Cipollina, G. Micale, M. Ciofalo, Pressure drop at low Reynolds numbers in woven-spacer-filled channels for membrane processes : CFD prediction and experimental validation, Desalin. Water Treat. 61 (2017) 170–182. doi:10.5004/dwt.2016.11279.

SUPPLEMENTARY MATERIALS

S1. Reverse Electrodialysis model

S1.1. Low-hierarchy model

The RED model consists of different sub-models, which are inter-connected according to a hierarchical structure. The low-hierarchy model presented in this section is relevant to the *cell pair*, which is schematically represented in Figure S 1.

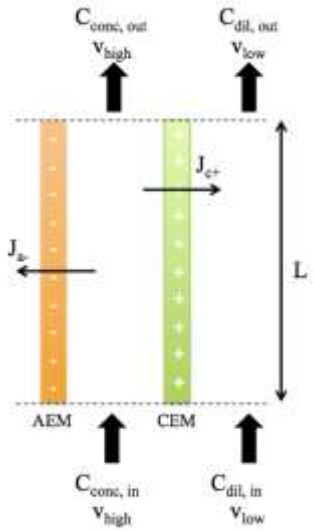

Figure S 1. Schematic representation of the cell pair.

This is a distributed-parameter model along the length of the channels. The length L is discretized in 50 elements, thus allowing evaluating the variation of each distributed variable along the channel length. Note that a sensitivity analysis was preventively performed to ensure results independence from the discretization degree adopted. For sake of brevity, the analysis is not reported in the present work but it was widely documented in [60]. The model contains all fundamental correlations describing the physical (e.g. density, conductivity, viscosity) and the thermodynamic properties of the solutions (e.g. the activity and osmotic coefficients). Mass balances include all fluxes (i.e. ions, salt and water fluxes) occurring across the IEMs. Finally, the potential difference generated by the cell pair is evaluated. Models equations are reported in the following.

Starting from the properties of the solutions, the Pitzer model has been employed to evaluate the activity and the osmotic coefficients of the pure salts in water [61].

The solution equivalent conductivity is calculated through the Jone and Dole's equation [62]:

$$\Lambda\,(x) = \Lambda_0 - \frac{A_\Lambda \sqrt{\frac{C_{salt}(x)}{1000}}}{1 + B_\Lambda \sqrt{\frac{C_{salt}(x)}{1000}}} - C_\Lambda \frac{C_{salt}(x)}{1000} \quad \text{(S. 1)}$$

where:

Λ is the equivalent conductivity of the salt solution [mS l/(mol cm)];

Λ_0 is the equivalent conductivity of the salt solution at infinite dilution;

A_Λ, B_Λ and C_Λ are the parameters specific for each salt;

C_{salt} is the molar concentration of the salt [mol/m^3].

Knowledge of the solution conductivity allows the estimation of the electrical resistance of the concentrate and the dilute channels:

$$R_{high}(x) = s_f \frac{\delta_{high}}{\Lambda_{high}(\mathrm{x}) C_{high}(\mathrm{x})} \frac{1}{A} 10^4 \quad \text{(S. 2)}$$

$$R_{low}(x) = s_f \frac{\delta_{low}}{\Lambda_{low}(\mathrm{x}) C_{low}(\mathrm{x})} \frac{1}{A} 10^4 \quad \text{(S. 3)}$$

where:

s_f is the spacer shadow factor, a geometric constant that takes into account the presence of a non-conductive spacer inside the channel, which determines an increase of the compartment resistance. It is taken equal to 1.5625 [60];

A is the membrane area;

δ_{low} and δ_{high} are the thicknesses of the spacers used in the dilute and in the concentrate compartment, respectively.

Membrane resistances are estimated through empirical correlations, derived from experimental data obtained for FujiFilm® membranes (E1 type, 150 μm thick) in NaCl-water solutions [63]:

$$R_{AEM}(x) = \left(0.487 \left(\frac{C_{high}(x)}{1000}\right)^2 - 2.81 \frac{C_{high}(x)}{1000} + 7.21 - 0.14 \frac{C_{low}(x)}{1000}\right) \frac{1}{A}\, 10^{-4} \quad \text{(S. 4)}$$

$$R_{CEM}(x) = \left(0.487 \left(\frac{C_{high}(x)}{1000}\right)^2 - 2.81 \frac{C_{high}(x)}{1000} + 7.22 - 0.27 \frac{C_{low}(x)}{1000}\right) \frac{1}{A} 10^{-4} \quad \text{(S. 5)}$$

where C_{high} and C_{low} are the concentrations of the concentrate and the dilute solution respectively [mol/m^3]. Then, the resistance of the cell pair can be estimated as follows:

$$R_{cell}(x) = R_{AEM}(x) + R_{CEM}(x) + R_{high}(x) + R_{low}(x) \quad \text{(S. 6)}$$

The other electrical variable defined within the cell pair model is the potential difference generated by the cell pair. This is estimated according to the Nernst potential equation [64], in which the ideal potential difference (E_{cell}) is corrected considering the membranes mean permselectivity (α_{av}) and the polarisation coefficients θ.

$$E_{cell}\,(x) = 2\,\alpha_{av}(\mathrm{x})\,\frac{R\,T}{F}\ln\left(\theta_{high}(\mathrm{x})\,\theta_{low}(\mathrm{x})\,\frac{\gamma_{high}(\mathrm{x})\,C_{high}(\mathrm{x})}{\gamma_{low}(\mathrm{x})\,C_{low}(\mathrm{x})}\right) \quad \text{(S. 7)}$$

The membrane permselectivity was evaluated through empirical correlations, derived for the same membranes (FujiFilm® E1 type membranes):

$$\alpha_{AEM}(x) = 0.987 - 0.0441\,\frac{C_{high}(x)}{1000} - 0.183\,\frac{C_{low}(x)}{1000} \quad \text{(S. 8)}$$

$$\alpha_{CEM}(x) = 0.991 - 0.0441\,\frac{C_{high}(x)}{1000} - 0.253\,\frac{C_{low}(x)}{1000} \quad \text{(S. 9)}$$

The polarisation coefficients were calculated implementing suitable correlations, obtained through CFD simulations for the case of flat membranes and Deukum spacers [65].

$$\theta_{low}(x) = \left(1 + \left(\frac{2\,J_{migr}(x)\,\delta_{low}}{Sh_{low}(x)\,D_{low}\,C_{low}(x)}\right)\right)^{-1} \quad \text{(S. 10)}$$

$$\theta_{high}(x) = 1 - \left(\frac{2\,J_{migr}(x)\,\delta_{high}}{Sh_{high}(x)\,D_{high}\,C_{high}(x)}\right) \quad \text{(S. 11)}$$

where:

δ_{high} and δ_{low} are the thicknesses of the spacers used in the concentrate and in the dilute channel respectively. They are both set equal to 150 microns;

D_{high} and D_{low} are the salt diffusivity values in the concentrate and in the dilute channel respectively, considered constant and equal to 1.5E-9 m^2/s;

J_{migr} is evaluated through equation (S. 13);

Sh_{high} and Sh_{low} are the Sherwood numbers, relevant to the concentrate and the dilute solutions, which are calculated as functions of the Reynolds numbers Re_{high} and Re_{low}, respectively [47,66]:

$$Sh(x) = -2E(-9)\,Re(x)^6 + 4E(-7)\,Re(x)^5 - 2E(-5)\,Re(x)^4 - 0.0005\,Re(x)^3 + 0.0509\,Re(x)^2 + 0.6125\,Re(x) + 6.2591 \quad \text{(S. 12)}$$

As far as the fluxes are concerned, three fluxes are accounted for:

(i) the counter-ion migrative flux across the membrane (J_{migr});

(ii) the diffusive salt flux through the membrane (J_{diff}), which is linked with the non-ideal permselectivity of the membrane;
(iii) the water flux (J_w) given by the sum of the osmotic flux (J_{osm}), due to the difference of osmotic pressure on the two sides of the membrane, and the electro-osmotic flux (J_{eosm}) [67]. These are defined as in the equations (S. 13)-(S. 17) respectively.

$$J_{migr}(x) = \frac{j(x)}{F} \tag{S. 13}$$

$$J_{diff}(x) = 2\,\frac{D_{salt}^{membr}}{\delta_{membr}}\left[C_{high}(x) - C_{low}(x)\right] \tag{S. 14}$$

$$J_w(x) = J_{osm}(x) + J_{eosm}(x) \tag{S. 15}$$

$$J_{osm}(x) = -2\,L_P\,\Delta\Pi = -2\,L_P\left[\nu\,RT\left(\varphi_{high}(x)C_{high}(x) - \varphi_{low}(x)C_{low}(x)\right)\right] \tag{S. 16}$$

$$J_{eosm}(x) = n_h\,J_{tot}(x) \tag{S. 17}$$

where:
j is the ionic current density;
J_{tot} is the sum of the migrative and the diffusive flux;
D^{membr}_{salt} and δ_{membr} are the diffusivity of the salt through the membrane (equal to 10^{-12} m^2/s [4]) and the thickness of the membrane, respectively;
L_P is the water permeability coefficient of the membrane;
$\Delta\Pi$ is the osmotic pressure difference across the membrane;
n_h is the total hydration number for the cation and the anion set equal to 7 [4].

These fluxes appear in the mass balances (in the equations (S. 18)-(S. 19)), which are expressed in differential form [67]:

$$\frac{d\,C_{low}(x)}{dx} = \frac{b}{Q_{low}}\,J_{tot}(x) - C_{low}(x)\,\frac{b}{Q_{low}}\,J'_w(x) \tag{S. 18}$$

$$\frac{d\,C_{high}(x)}{dx} = -\frac{b}{Q_{high}}\,J_{tot}(x) + C_{high}(x)\,\frac{b}{Q_{high}}\,J'_w(x) \tag{S. 19}$$

where:
b is the membrane width;
Q_{low} and Q_{high} are the volume flow rates in the two compartments;
J'_w is the volumetric flux of water through the membranes.

S1.2. High-hierarchy model

The high-hierarchy model includes all the *cell pair* models and is relevant to the whole *stack* presented in Figure 3.

This larger scale model is devoted to calculating the main electrical outputs of the stack. In particular, as reported in the low-hierarchy model section, the unit length is discretized in 50 elements, acting as elements in parallel, each exposed to the same total potential difference E_{stack}. Thus, the current relevant to each single element can be derived from the Kirchhoff's loop rule on a generic loop including the branch corresponding to the single element and the external branch (containing R_{blank} and R_{ext}), as reported in equation (S. 22). Then, according to the Kirchhoff's nodal rule, the current circulating in the external circuit (whose resistance is R_{ext}) i_{stack} is given by the sum of all the currents i_{cell} (see the node reported in Figure S 2).

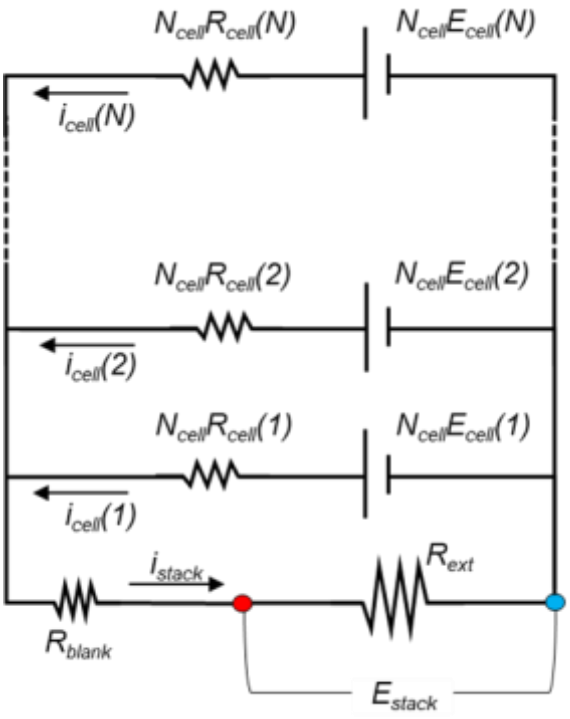

Figure S 2. Equivalent electrical scheme of the RED stack.

As it can be seen in the equivalent electrical scheme of the RED stack reported in Figure S.2, the manifolds (i.e. distributor and collector) along with their parasitic currents are not included. It is well known that their detrimental effect is higher the higher the number of cell-pairs. Also, its impact is dependent on the stack geometry: longer channels and manifolds with a low section are known to reduce the parasitic currents. We simulated in the past a similar geometry RED stack with the same number of cell

pairs (i.e. 50) by using a multi-scale model including also the parasitic current effect and a negligible effect was found [4].

The gross power density generated by the unit can be easily calculated as the product of the stack voltage times the corresponding circulating current. By letting R_{ext} to vary from 0 (short circuit condition) to infinite (OCV condition), the power density curve can be derived. As expected, the model confirms (not shown for brevity) that power density is maximized when stack resistance equals the external load [68].

The model includes an optimization routine which adopts the R_{ext} value maximizing the power output. It can be mathematically demonstrated that, at a given salinity gradient, power is maximized when $R_{ext} = R_{stack}$, while a difference is found in real units where a driving force depletion occurs along the channels. More precisely, in all units where the streamwise variation of solutions concentration (i.e. driving force reduction along the channels) is not significant, power output is maximized by the condition $R_{ext} = R_{stack}$. Conversely, when residence time is higher, the R_{ext} maximizing the power output is a bit higher than R_{stack}.

The main figures of the RED system are calculated according to equations (S. 20)-(S. 23).

$$E_{stack} = R_{ext}\, i_{stack} \tag{S. 20}$$

$$i_{stack} = \sum_{x=1}^{N} i_{cell}\,(x) \tag{S. 21}$$

$$i_{cell}(x) = \frac{N_{cell}\, E_{cell}(x) - \left(R_{ext}\, i_{stack} + {i_{stack} R_{blank}}/{A}\right)}{N_{cell}\, R_{cell}(x)} \tag{S. 22}$$

$$P_D = \frac{E_{stack}\, i_{stack}}{N_{cell}\, A} \tag{S. 23}$$

where:

R_{ext} is the electrical resistance of the external load [Ω];

N_{cell} is the number of cell pairs inside the stack;

A is the membrane area;

R_{blank} is the electrical resistance of the electrodic compartments (including the electrodes and the electrodic solutions) [Ω m^2], experimentally measured as reported in [63] and equal to 0.0327 Ω m^2;

P_d is the achievable power density [W/m^2].

The model also accounts for the distributed pressure drops. A relationship between the friction factor *f* and the Reynolds number *Re* was derived from the literature for flat membranes and Deukum spacers [69]:

$$f(x) = 148.44\ Re(x)^{-0.926} \tag{S. 24}$$

Corresponding pressure losses can be calculated as follows:

$$\Delta P(x) = \frac{f(x)\ \rho(x)\ v(x)^2}{\delta}\ \frac{L}{N} \tag{S. 25}$$

$$\Delta P_{tot} = \sum_{x=1}^{N} \Delta P(x) \tag{S. 26}$$

where ρ is the solution mass density, v is the fluid velocity along the channel length L, δ is the thickness of the spacer filling the channel, N is the number of elements in which the length is discretized.

Once pressure drops have been evaluated, it is possible to calculate the net power, as the difference between the total gross power produced (obtained multiplying the maximum power density by the total area) and the pumping power necessary for operation.

S2. Membrane Distillation model

S2.1. Current commercial MD modules

The distillate flow rate and the thermal consumption values shown in Figure S 3 were kindly provided by Aquastill on the basis of a validated model published by the same company [49]. Starting from these data, some simple correlations were built in order to simulate the behaviour of real vacuum-enhanced AGMD units. In particular, on the left, the values of distillate flow rate Q_D varying the concentration of the MD feed are reported for the two investigated MD unit lengths. Conversely, on the right, the corresponding values of specific thermal consumption are shown. It is evident that a longer stack ensures a higher heat recovery and requires lower amounts of thermal energy. Moreover, it is noticeable that the distillate flow rate decreases and the STC increases with the MD feed concentration, because of the deployment of the available vapour pressure difference.

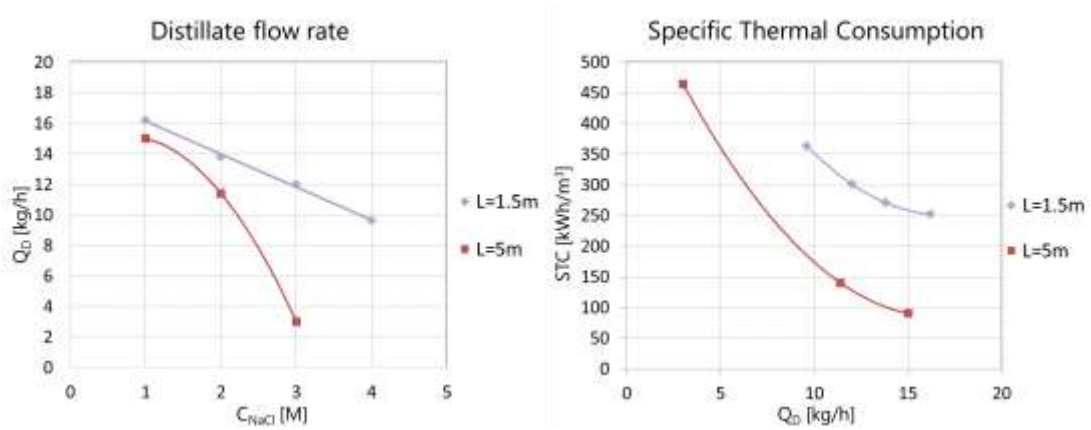

Figure S 3. Distillate flow rate Q_D as function of the concentration (left) and STC as function of the distillate flow rate (right) at two different MD unit lengths (1.5 m and 5 m) for a real MD unit.

The trends of Q_D vs. C_{NaCl} and STC vs. Q_D can be reliably fitted by a 2nd grade polynomial function:

$$f_u = a\,x^2 + b\,x + c \qquad \text{(S. 27)}$$

where fitting coefficients are reported in Table S 1.

	Module	a	b	c
Q_D vs C_{NaCl}	1.5	0	-2.16	18.3
	5	-2.4	3.6	13.8
STC vs Q_D	1.5	2.13	-71.84	856.03
	5	2.06	-68.29	650.3

Table S 1. Fitting coefficients for the correlations of Q_D vs. C_{NaCl} and STC vs. Q_D for real MD unit, according to the polynomial function in (S.27).

S2.2. Future MD modules

The results of the model simulations accounting for improved MD modules were also kindly provided by Aquastill. These results were employed to derive correlations, which were used to simulate the highly performing RED-MD cycle. In Figure S 4 (left), the trends of the distillate flow rate value (Q_D) produced by the MD unit for the two investigated cases (i.e. MD module length of 1.5 m and 5 m) are reported as a function of the solution concentration. In Figure S 4 (right), the trends of the STC vs. the distillate flow rate for the same two module lengths are shown.

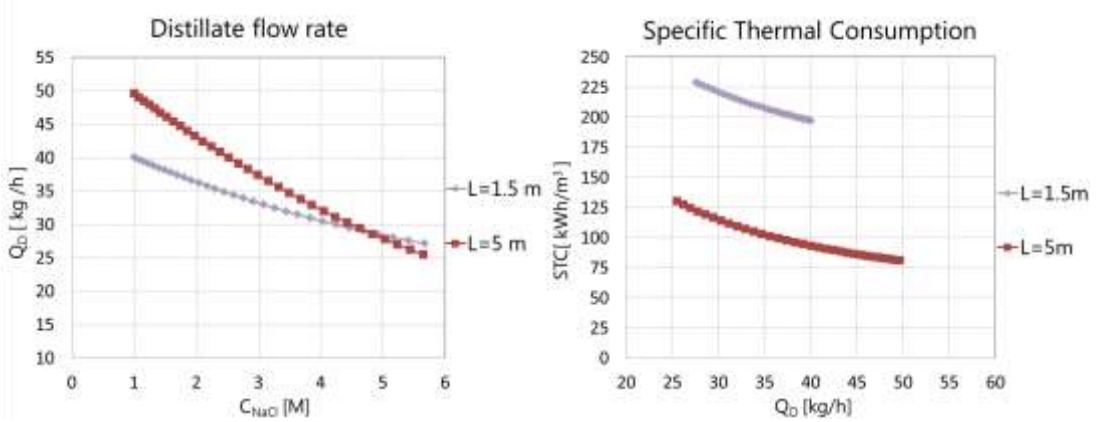

Figure S 4. Distillate flow rate Q_D as function of the concentration (left) and STC as function of the distillate flow rate (right) at two different MD unit lengths (1.5 m and 5 m) for a future MD module.

Also in this case, the trends of Q_D vs. C_{NaCl} and STC vs. Q_D can be reliably fitted by a 2nd grade polynomial function, as in (S.27), and the fitting coefficients for this case are reported in Table S 2.

	Module	a	b	c
Q_D vs C_{NaCl}	1.5	0.24	-4.35	44.1
	5	0.35	-7.55	56.77
STC vs Q_D	1.5	0.068	-7.15	374.17
	5	0.056	-6.21	250.96

Table S 2. Fitting coefficients for the correlations of Q_D vs. C_{NaCl} and STC vs. Q_D for highly performing MD unit, according to the polynomial function in (S.27).